International Journal of Fluid Power 11 (2010) No. 1 pp. 47-59

ANALYSIS AND CONTROL OF A WATER HYDRAULIC MANIPULATOR FOR ITER DIVERTOR REMOTE MAINTENANCE

Likui Zhai[1], Tapio Virvalo[1], Jouni Mattila[1] and Hannu Saarinen[1,2]

[1]*Department of Intelligent Hydraulics and Automation, Tampere University of Technology, Tampere, Finland*
[2]*VTT Technical Research Centre of Finland, Tampere, Finland*
likui.zhai@gmail.com, tapio.virvalo@gmail.com, jouni.mattila@tut.fi, hannu.saarinen@vtt.fi

Abstract

This paper focuses on the analysis and control of a water hydraulic manipulator, which is specific for the International Thermonuclear Experimental Reactor (ITER) cassettes' (each weighing 10 tonnes) maintenance tasks. The manipulator comprises a closed-chain main body and an open-chain end-effector. Following a systematic way of analyzing differential kinematics and vibration modes, it is revealed that from a control point of view the manipulator faces two main restrictions. The first one is that the closed-chain structure degrades tracking performances, rising from kinematic coupling. Secondly, as the end-effector drives a very high inertial load instead of a gravitational load, small actuators are used, resulting in low system natural frequency and damping. To solve the first issue, a kinematic model-based decoupling controller is designed. Moreover, to improve the steady-state accuracy in spite of low frequency and damping, acceleration feedback is adopted, achieving higher damping and position loop gains. Experimental results show that decoupling controller brings five times smaller tracking errors, while acceleration feedback controller reaches three times better accuracies than proportional controller. This study also confirms that in spite of using commercially available water hydraulic components, the achieved positioning accuracies and dynamic behavior are competitive with oil hydraulics.

Keywords: hydraulic manipulator, coupling, kinematic model-based decoupling, vibration mode analysis, ITER

1 Introduction

ITER is a large-scale scientific experiment aiming to demonstrate the scientific and technological feasibility of fusion energy for commercial energy production (Rebut, 1995). The divertor area of ITER comprises 54 rail-mounted cassettes. Due to the erosion of the plasma-facing components and possible need for improving the design of critical items, these cassettes must be periodically replaced and refurbished every 3-4 years during ITER's 20 years operational time (Palmer et al., 2005). Each cassette has an estimated mass of 10 tonnes with an external dimension of 3.5 m length by 2.0 m height by 0.8 m width. To execute these cassettes remote maintenance tasks, one of the most competitive solutions is to utilize the advantages of hydraulics (high power density, large force/torque, high load stiffness) together with pure water as the pressure medium (nonflammable, chemically neutral and irradiation resistant) (Raneda et al., 2003).

The installation (or removal) of the cassettes has a motion characteristic that the position change is mainly in a vertical plane, while the orientation varies mostly in a near horizontal plane. Therefore, the designed water hydraulic manipulator comprises a closed-chain main body (so-called Cassette Multi-functional Mover, CMM) and an open-chain end-effector (so-called Second Cassette End-Effector, SCEE) (see Fig. 1). The CMM provides lifting and tilting motions in the vertical plane, with its closed-chain structure improving system stiffness. The SCEE, which consists of cantilever (CRO) and hook-plate (HRO) rotational joints, is mainly devoted to change the cassette's orientation. Lastly, with the aid of electric motor drive, CMM may radially travel on the top of the maintenance tunnel rails.

This manuscript was received on 28 October 2009 and was accepted after revision for publication on 14 January 2010

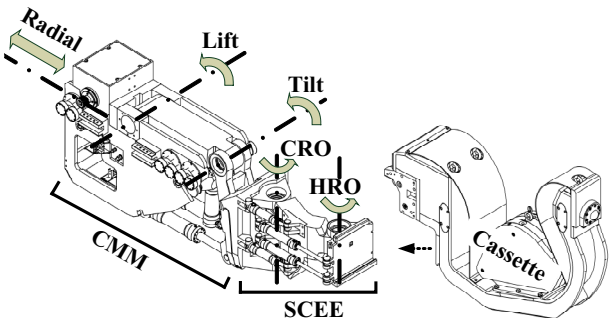

Fig. 1: *CMM/SCEE and a second cassette*

During the installation (or removal) process, in order to avoid any collisions to the surroundings, very high steady-state and follow-up accuracies are desired. The typical desired accuracies are ± 0.07 degree in joint space. Another requirement is to have reasonably fast response, so a bandwidth of 0.5 Hz is selected.

Like electrical robot manipulators, controlling hydraulic manipulators may use decentralized or centralized control scheme depending on the applications. When the manipulators needs to be controlled at high speed and large bandwidth, the dynamic coupling effects between joints are not negligible, whereas centralized control methods, such as computed torque feedforward control (Wang et al., 2009), inverse dynamics control (Plummer, 2007; Davliakos and Papadopoulos, 2008) and adaptive control (Sirouspour and Salcudean, 2001) have been widely studied. On the other hand, if the manipulators work at low speed and small bandwidth, decentralized control could be adopted, which regards the manipulator as n independent system (n joints) and coupling effects as disturbances (Gunnarsson and Krus, 1994; Edge and Gomes de Almeida, 1995; Gizatullin and Edge, 2006; Guo et al., 2008). For this cassette installation (or removal) process, the desired bandwidth is 0.5 Hz and every joint receives smooth trajectory input of low speed (< 1 deg/s). Therefore, decentralized control approach is utilized to simplify controller design.

In order to analyze how the each joint vibrates and at which natural frequencies, vibration modes analysis becomes important. Linjama and Virvalo (1999) have analyzed the vibration modes of a flexible hydraulic crane to assist controller design. Plummer (2004) has used the vibration modes analysis to optimize the design of a parallel manipulator. In this paper, vibration modes analysis shows CRO joint exhibits very low natural frequency which restricts the desired accuracy. Therefore, to improve the steady-state accuracy, acceleration feedback is adopted, achieving higher damping and position loop gains.

The tracking performances of closed-chain manipulators are very often limited by the kinematic coupling. Besides individual speed feedforward, many researchers have tried to add integrator term to improve the tracking accuracy (Fales, R. 2004; Rokala, 2007). However, this may lead to hunting problem (Virvalo, 2001). In this paper, a kinematic model-based decoupling controller is proposed and tested.

Despite the aforementioned control problems, using water as pressure medium leads to additional issues. So far the choice for water hydraulic components is very limited, and their characteristics are usually worse than those of oil hydraulics. Therefore, this study is also important to (experimentally) confirm that the designed water hydraulic manipulator is competitive with their oil hydraulic counterpart.

Because the manipulator moves at low speed and the motion of lift-tilt mechanism is orthogonal to that of CRO-HRO, for simplicity of later analysis they are regarded as two independent 2DOF systems (see Fig. 2). The rest of the paper is organized as follows: Section 2 presents the kinematic analysis which reveals kinematic coupling in the closed-chain structure. Dynamic model is derived in section 3 and then used for static force and vibration modes analysis. Section 4 introduces the test system and verifies the vibration modes analysis by open loop velocity responses. The design and experimental results of both feedback and feedforward controllers are presented in section 5. The conclusions are drawn in the last section.

2 Kinematic Analysis

Figure 2 presents a schematic diagram of the studied manipulator with defined link frames, following a typical convention (Sciavicco and Siciliano, 2000). The Denavit-Hartenberg parameters are specified in Table 1, where θ_i denotes the manipulator joint angel between two incident normals of a joint axis, a_i – the length of link i, α_i – twist angle between two adjacent joint axes, d_i – translational distance between two incident normals of a joint axis (Tsai, 1999).

Table 1: Denavit-Hartenberg parameters of CMM/SCEE

Link	a_i [m]	α_i [rad]	d_i [m]	θ_i [rad]
1	0	0	d_1	0
2	$-a_1$ (-0.165)	$\pi/2$	d_{1v} (0.795)	$3\pi/2+\theta_2$
3	a_2 (1.202)	0	0	θ_3
4	a_3 (0.701)	$-\pi/2$	$-d_4$ (-0.026)	θ_4
5	a_4 (0.950)	0	0	θ_5

The joint-to-Cartesian direct kinematic transformation can be constructed from the homogenous transformation matrices by matrix multiplication

$$\boldsymbol{y} = \boldsymbol{h}_1(\boldsymbol{\theta}) = \boldsymbol{A}_1^0(d_1)\boldsymbol{A}_2^1(\theta_2)\boldsymbol{A}_3^2(\theta_3)\boldsymbol{A}_4^3(\theta_4)\boldsymbol{A}_5^4(\theta_5) \qquad (1)$$

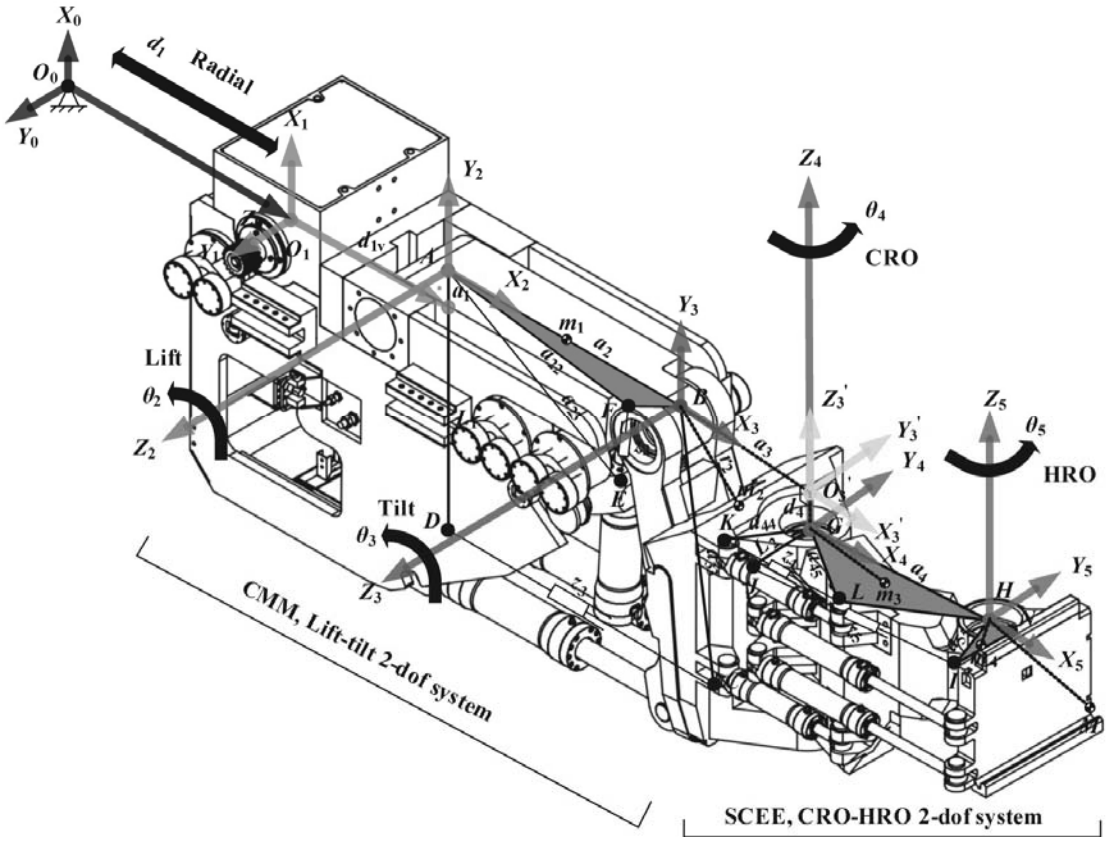

Fig. 2: *Schematic diagram of the CMM/SCEE*

where $\boldsymbol{y}$ – the position vector in Cartesian coordinate, $\boldsymbol{A}_{\mathrm{i}}^{\mathrm{i-1}}$ - the homogenous transformation matrix

$$\boldsymbol{A}_{\mathrm{i}}^{\mathrm{i-1}}(\theta_{\mathrm{i}}) = \begin{bmatrix} c\theta_{\mathrm{i}} & -s\theta_{\mathrm{i}}c\alpha_{\mathrm{i}} & s\theta_{\mathrm{i}}s\alpha_{\mathrm{i}} & a_{\mathrm{i}}c\theta_{\mathrm{i}} \\ s\theta_{\mathrm{i}} & c\theta_{\mathrm{i}}c\alpha_{\mathrm{i}} & -c\theta_{\mathrm{i}}s\alpha_{\mathrm{i}} & a_{\mathrm{i}}s\theta_{\mathrm{i}} \\ 0 & s\alpha_{\mathrm{i}} & c\alpha_{\mathrm{i}} & d_{\mathrm{i}} \\ 0 & 0 & 0 & 1 \end{bmatrix} \tag{2}$$

The notations $s\theta_{\mathrm{i}}$ and $c\theta_{\mathrm{i}}$ are the abbreviations for $\sin\theta_{\mathrm{i}}$ and $\cos\theta_{\mathrm{i}}$.

In a compact form, the differential kinematic equation can be written as

$$\boldsymbol{v} = \boldsymbol{J}(\boldsymbol{\theta})\dot{\boldsymbol{\theta}} \tag{3}$$

where $\boldsymbol{J}$ - the joint-to-Cartesian Jacobian matrix, $\dot{\boldsymbol{\theta}}$ - the joint velocity vector, and $\boldsymbol{v}$ – the velocity vector in Cartesian coordinate.

Similarly, the joint-to-actuator transformation and corresponding differential kinematic equation can be expressed as

$$\boldsymbol{z} = \boldsymbol{h}_2(\boldsymbol{\theta}) \tag{4}$$

$$\dot{\boldsymbol{z}} = \boldsymbol{A}_{\mathrm{h}}(\boldsymbol{\theta})\dot{\boldsymbol{\theta}} \tag{5}$$

where $\boldsymbol{A}_{\mathrm{h}}$ - the joint-to-actuator Jacobian matrix, $\boldsymbol{z}$ – the cylinder length vector, and $\dot{\boldsymbol{z}}$ – the cylinder velocity vector.

Detailed kinematic equations for both lift-tilt and CRO-HRO 2DOF systems are presented in the appendix.

From Eq. 21 in the appendix, the tilt joint velocity $\dot{\theta}_3$ is a function of both lift cylinder velocity $\dot{z}_2$ and tilt cylinder velocity $\dot{z}_3$

$$\dot{\theta}_3 = \frac{1}{A_{\mathrm{hLT22}}}\dot{z}_3 - \frac{A_{\mathrm{hLT21}}}{A_{\mathrm{hLT11}}A_{\mathrm{hLT22}}}\dot{z}_2 \tag{6}$$

In other words, tilt joint velocity is affected by both tilt and lift cylinder velocities. This effect rises from the kinematic coupling of the closed-chain structure in the lift-tilt 2DOF system. This coupling will decrease the tracking performance of tilt joint which is discussed in section 5.2 and 5.3. By comparison, no such kinematic coupling exists in the open-chain CRO-HRO 2DOF system.

3 Dynamic Analysis

3.1 Dynamic Motion Equation

Neglecting joint friction and disturbance terms, the dynamic equation of the mechanical mechanism can be derived based on Lagrange's formulation

$$\boldsymbol{M}(\boldsymbol{\theta})\ddot{\boldsymbol{\theta}} + \boldsymbol{V}(\boldsymbol{\theta},\dot{\boldsymbol{\theta}}) + \boldsymbol{G}(\boldsymbol{\theta}) = \boldsymbol{\tau} = \boldsymbol{A}_{\mathrm{h}}^{\mathrm{T}}\boldsymbol{F}_{\mathrm{h}} \tag{7}$$

where $\boldsymbol{M}$ is the inertia matrix, $\boldsymbol{V}$ is the matrix of centrifugal and Coriolis terms and $\boldsymbol{G}$ is the gravitational torque vector (Sciavicco and Siciliano, 2000). Centrifugal and Coriolis forces are neglected in this study, because the angular velocities are rather low.

The inertia matrix is a sum of individual inertia matrices

$$\boldsymbol{M}(\boldsymbol{\theta}) = \sum_{i=1}^{n} m_{l_i} \boldsymbol{J}_P^{(l_i)T} \boldsymbol{J}_P^{(l_i)} \tag{8}$$

The vector of generalized toque is expressed as

$$\boldsymbol{G}(\boldsymbol{\theta}) = \sum_{i=1}^{n} m_{l_i} \boldsymbol{g}_0^T \frac{\partial \boldsymbol{p}_{l_i}}{\partial \theta_i} \tag{9}$$

For each 2DOF system, the derived dynamic equation terms are presented in the appendix.

3.2 Effect of Gravitational Torque on the Lift-Tilt 2DOF System

The non-zero gravitational torque in the lift-tilt 2DOF system affects both steady state accuracy Δy and actuator space velocity gain K_{qa_cyl}.

Figures 3 and 4 show the static actuating force on the lift and tilt cylinder in the whole working range. The force variations are 28 kN (115 ~ 143 kN) for lift joint and 61 kN (138 ~ 199 kN) for tilt joint. These results are used for tuning offsets of the servo valves to compensate gravitational torque.

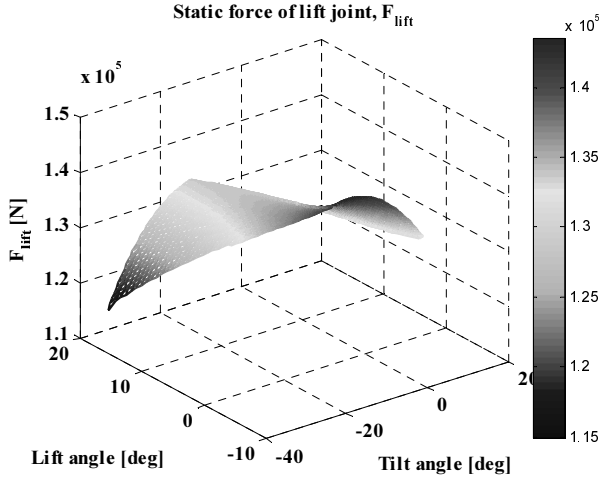

Fig. 3: *Static force on lift cylinder*

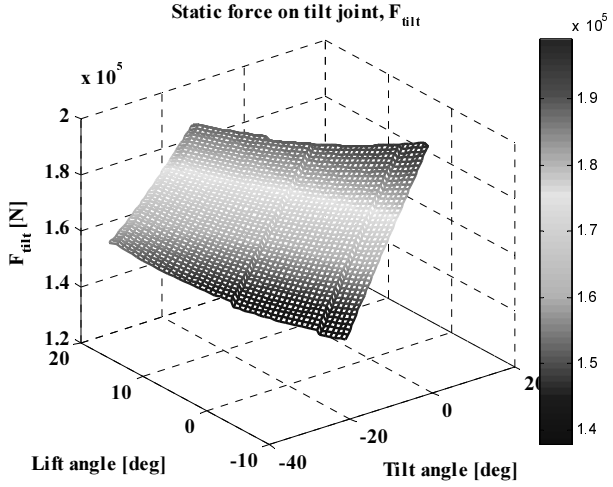

Fig. 4: *Static force on tilt cylinder*

The velocity gains in actuator space are strongly affected by gravitational torque; in this case K_{qa_cyl} in retraction direction is around 1.4 times bigger than that of extension direction for both joints. Even in the same direction the maximum variation of K_{qa_cyl} is found to be as much as 11.5 % for lift joint and 9.2 % for tilt joint.

3.3 Vibration Mode Analysis

The vibration mode consists of the mode shape, which shows how the system vibrates, and the corresponding natural frequency. The vibration modes for the studied hydraulic manipulator are calculated by only considering the hydraulic fluid compressibility, ignoring linkage flexibility and joint clearances.

Thus the undamped eigenvalue problem of free vibration is analyzed; utilizing the linear model of the mechanism (Linjama, 1998):

$$\boldsymbol{M}_0 \Delta\ddot{\boldsymbol{\theta}} + \boldsymbol{K}_0 \Delta\boldsymbol{\theta} = 0 \tag{10}$$

The notations $\boldsymbol{M}_0(\boldsymbol{\theta}_0) = \boldsymbol{M}_0$, $\boldsymbol{A}_{h0}(\boldsymbol{\theta}_0) = \boldsymbol{A}_{h0}$ are adopted to clarify the equations.

The stiffness matrix $\boldsymbol{K}_0$ is expressed as

$$\boldsymbol{K}_0 = \boldsymbol{A}_{h0}^T \mathrm{diag}(K_{hj}) \boldsymbol{A}_{h0} \tag{11}$$

where $\mathrm{diag}(K_{hj})$ is an $n \times n$ diagonal matrix of hydraulic spring constants (Merritt, 1967).

The natural frequencies are derived by

$$\omega_k = \sqrt{\lambda_k \{\boldsymbol{M}_0^{-1} \boldsymbol{K}_0\}} \tag{12}$$

where $\lambda_k\{\cdot\}$ is the k:th sorted eigenvalue of $\{\cdot\}$ and ω_k is the k:th natural frequency. The nonlinearity of the mechanism and actuator dynamics cause natural frequencies to depend strongly on the position and orientation of the manipulator. Figures 5 and 6 illustrate the first and second natural frequencies of the lift-tilt 2DOF system, where the lowest natural frequency is around 5 Hz. The first and second natural frequencies of the CRO-HRO 2DOF system are illustrated in Fig. 7 and 8, with lowest natural frequency around 1 Hz.

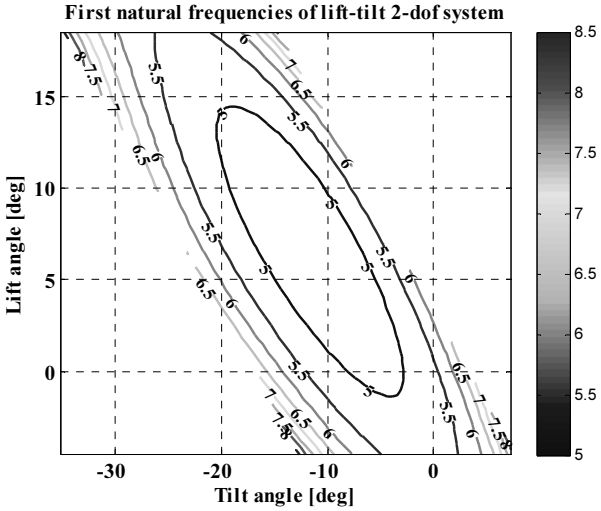

Fig. 5: *First natural frequencies of lift-tilt 2DOF system*

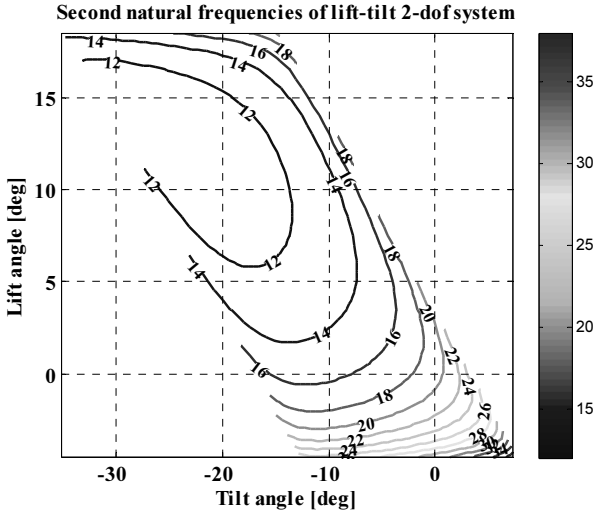

Fig. 6: *Second natural frequencies of lift-tilt 2DOF system*

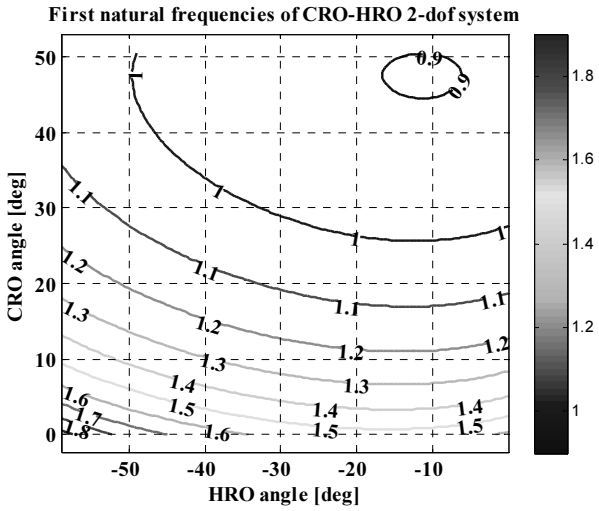

Fig. 7: *First natural frequencies of CRO-HRO 2DOF system*

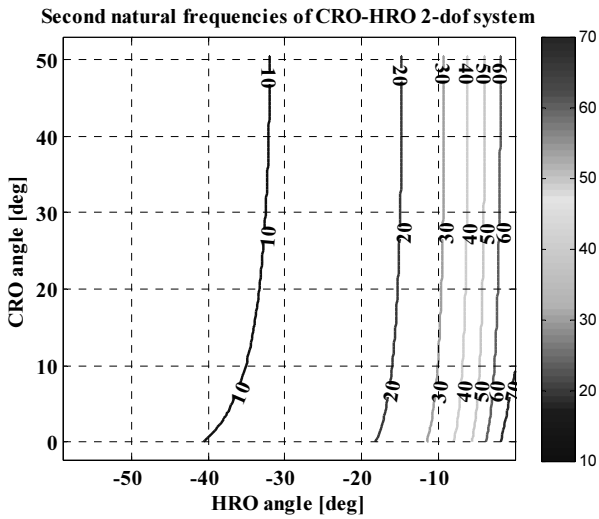

Fig. 8: *Second natural frequencies of CRO-HRO 2DOF system*

4 Test System and Open-Loop Tests

4.1 Test System

A photograph of the experimental setup is given in Fig. 9, where CMM/SCEE carries a 10 tonnes dummy load. The main specifications are listed as follows:

- Supply pressure p_S = 140 bar
- Servo valve: Moog 30-417
  Nominal flow Q_N 6.9 l/min with the nominal pressure drop 35 bar /control notch
  Rated current u_{max} = 10 mA
  Hysteresis < 3 %
  Null point leakage < 4 % (Q_N, Δp_N)
  Pressure gain $K_{pg} = (0.4 \times p_S) / (1.2\ \% \times u_{max})$
  90° bandwidth > 100 Hz
- Lift cylinder 125 / 80-430
- Tilt cylinder 125 / 80-470
- CRO cylinder 63 / 40-282
- HRO cylinder 63 / 40-395
- Resolver resolution: 0.0055 deg (16 bit)
- Sampling time: 2 ms

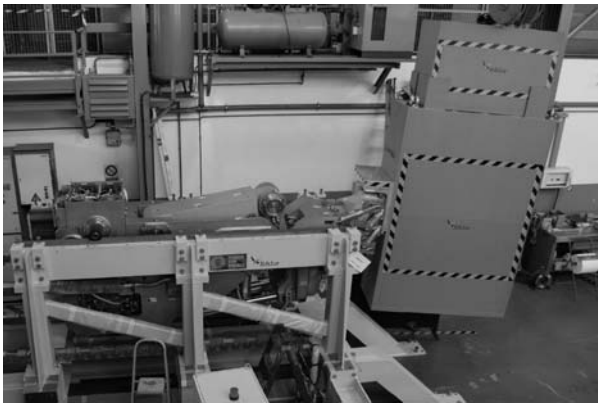

Fig. 9: *CMM/SCEE carrying a 10 tonnes test load*

4.2 Open Loop Tests

Hydraulic position systems are generally described by a third order model with parameters natural frequency ω_n, damping ratio δ_n and velocity gain K_{qa}; therefore the transfer function between valve input and velocity output is of second order. Furthermore, these three system parameters can be identified by analyzing the open loop velocity responses of step valve input. Figures 10 and 11 present the open loop test results of tilt and lift joints where θ_{tilt}=-15 deg, θ_{lift}= 10 deg, θ_{CRO}= 0 deg and θ_{HRO}= 0 deg.

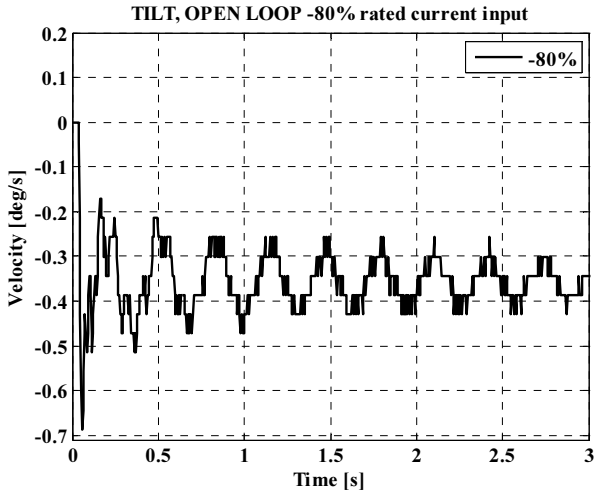

Fig. 10: *Open loop velocity responses of tilt joint*

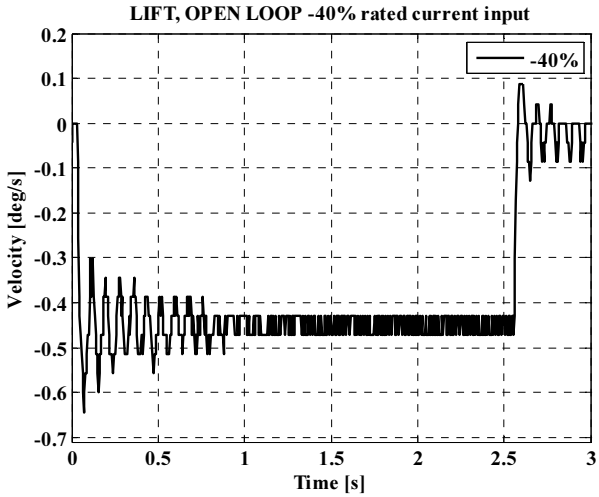

Fig. 11: *Open loop velocity responses of lift joint*

Similarly the open loop test results of CRO and HRO joints are shown in Fig. 12 and 13 where θ_{tilt}=-15 deg, θ_{lift}= 10 deg, θ_{CRO}= 40 deg and θ_{HRO}= -20 deg.

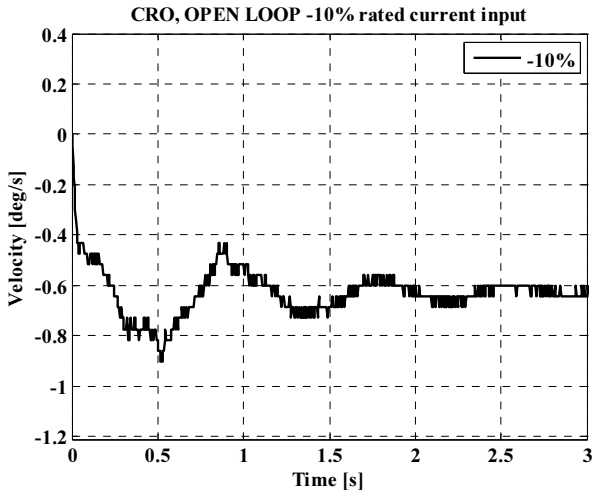

Fig. 12: *Open loop velocity responses of CRO joint*

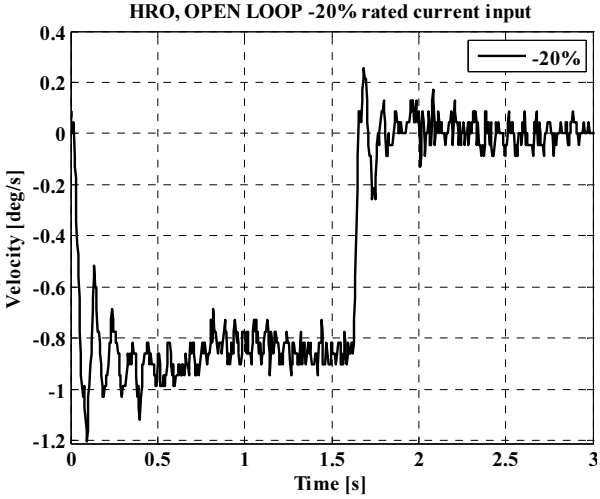

Fig. 13: *Open loop velocity responses of HRO joint*

For the lift-tilt 2DOF system by comparing Fig. 5 and 6 with Fig 10 and 11, it can be seen that the velocity responses of the tilt joint have a combination of the first and second vibration modes, and is dominated by the first natural frequency. The lift joint responses are mostly dominated by the second natural frequency. Similarly, for the CRO-HRO 2DOF system, Fig. 12 and 13 show that the first natural frequency is the dominating frequency for the CRO joint, while the second one is for the HRO joint. When the open loop tests are carried out at other positions and orientations, the same conclusion can be still be drawn with varied natural frequencies.

5 Controller Design and Experimental Results

5.1 System Requirements

The smallest clearance between the cassette and the service port (floor and ceiling) is about 20 mm, requiring a very high positioning accuracy (typical desired accuracy $\leq \pm$ 0.07 deg in joint space).

One practical performance specification for this kind of position feedback system may include a desired bandwidth ω_{BW}, an allowable steady-state and tracking errors Δy and a peak magnitude of closed loop frequency response M_{r}. For this application, the specifications are: $\omega_{\text{BW}} \geq 3$ rad/s, $\Delta y \leq 0.05$ deg and $M_{\text{r}} \leq 1$ dB.

The steady state position accuracy Δy is mostly affected by valve hysteresis H/100 (< 3 %) and external force F_{L}. The desired steady state accuracy Δy defines the desired position feedback gain KP_{des}

$$KP_{\text{des}} = u_{\max} \cdot \left(\frac{H}{100 \cdot \Delta y} + \frac{F_{\text{L}}}{20(A_1 + A_2)p_{\text{S}} \cdot \Delta y}\right) \qquad (13)$$

where $u_{\max}$ denotes rated valve input, A_1, A_2 - the areas of cylinder piston and rod sides, p_{s} – supply pressure. In this case, the estimated KP_{des} is 3 mA/deg.

Regarding position system as a linear third order transfer function, a rule of thumb to estimate position feedback gain KP with $M_{\text{r}} \leq 1$ dB is

$KP = 2 \cdot \delta_n \cdot \omega_n / (3K_{qa})$ (Virvalo and Mattila, 2007). The estimated KP for the four joints are $KP_{tilt} = 13$ mA/deg, $KP_{lift} = 18$ mA/deg, $KP_{CRO} = 1.6$ mA/deg, $KP_{HRO} = 15$ mA/deg. Comparing them with the desired position feedback gain KP_{des}, it is foreseen that it is relatively easy to achieve high steady-state accuracy for lift, tilt and HRO joints, but not for CRO joint.

5.2 Controller Design for Lift-Tilt 2DOF System

Based on the estimation in the previous section, phase lag P-controller (or phase lag compensator) is selected as the lift and tilt joint controller. The design methods are presented as follows.

$$C_i(s) = \frac{KP_i}{\tau_i s + 1}$$
$$\tau_i = 2 / \omega_{ni,min} \qquad (14)$$
$$KP_i = 1/(K_{qai} \cdot 5 \cdot \tau_i)$$

In this case, the lowest natural frequency is chosen to be 3.5 Hz for both controller design of Eq. 14, which significantly decreases the coupling effects and still achieves desired steady-state accuracy. The tuned position loop gains for both joints are listed in Table 2.

Table 2: Main controller gains for four joints

	KP_p [mA/deg]	KP_n [mA/deg]	K_a [mA·s^2/deg]
HRO	4.2	5.2	0
CRO	3.2	3.6	0.013
Tilt	40	17	0
Lift	24	10	0

Step responses of both joints are presented in Fig. 14 and 15. The steady state position errors are less than ± 0.01 deg for both joints.

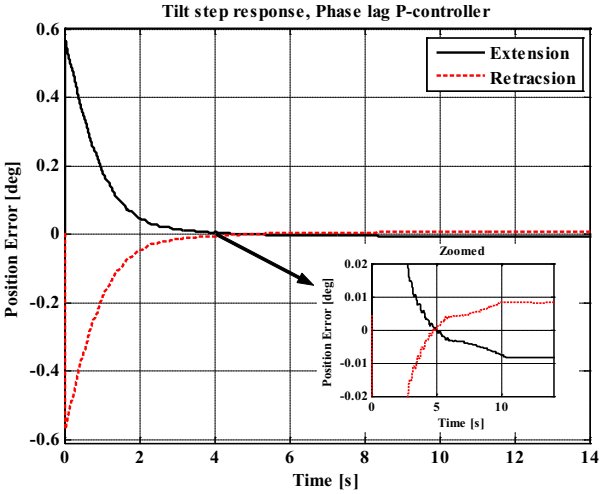

Fig. 14: *Position error responses of tilt joint (Phase lag P-controller, step)*

To improve the tracking performance, individual velocity feedforward gains are tuned for lift and tilt joints, $P_{dlift} = 9.6$ mA·s/deg, $P_{dtilt} = 21$ mA·s/deg. First the lift joint is kept stationary and tracking performances of the tilt joint are analyzed ($\dot{\theta}_{lift} = 0$ deg/s, $\dot{\theta}_{tilt} = \pm 0.05$ deg/s). Fig 16 shows the position and position error responses of tilt joint. It can be seen that the steady state error is very small (< 0.01 deg) and tracking errors are less than ± 0.025 deg (velocity/tracking error = 2 deg/s/deg). Steady state error of lift joint is also very small (< 0.01 deg), and the motion of tilt joint has no effect on lift joint.

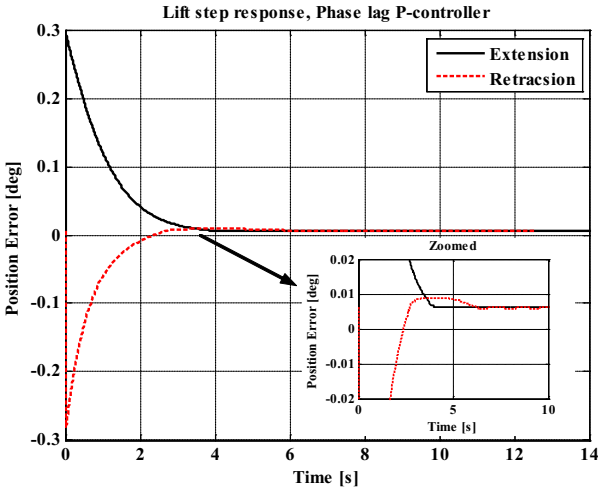

Fig. 15: *Position error responses of lift joint (Phase lag P-controller, step)*

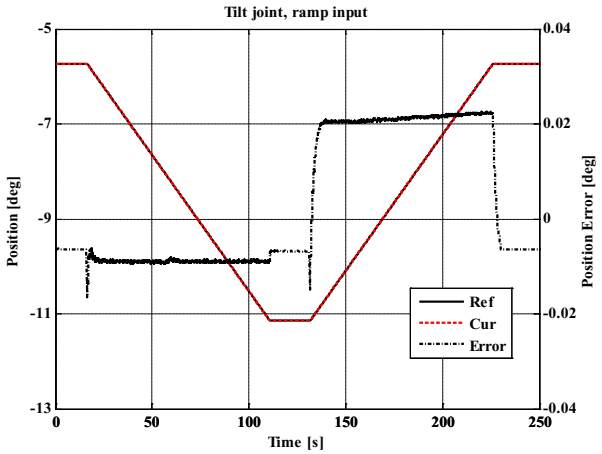

Fig. 16: *Position and position error responses of tilt joint (lift stationary)*

Then tilt angle is kept stationary and the tracking performances of both joints are analyzed ($\dot{\theta}_{lift} = \pm 0.1$ deg/s, $\dot{\theta}_{tilt} = 0$ deg/s). Figures 17 and 18 show the position and position error responses of lift and tilt joints. It can be seen that the tracking errors are less than ±0.03 deg (velocity/tracking error = 3.3 deg/s/deg) for lift joint, however, the tracking errors of tilt joint are as big as ± 0.1 deg (velocity/tracking error = 1 deg/s/deg). The reason of this is the kinematic coupling rising from the closed-chain structure (see Eq. 5 in section 2). To improve the follow-up accuracies of the tilt joint, a kinematic model based-decoupling controller is designed in the next section.

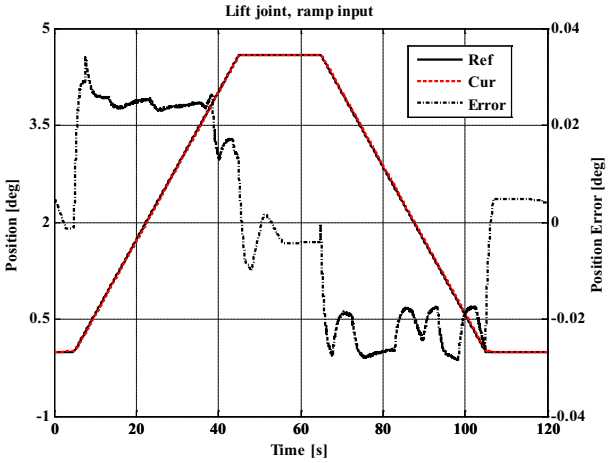

Fig. 17: *Position and position error responses of lift joint (coupled tracking)*

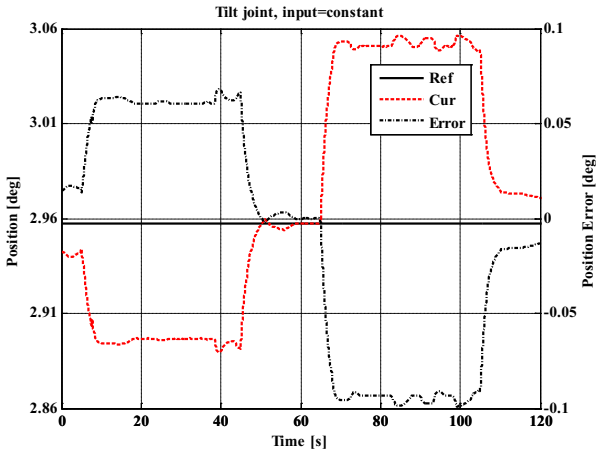

Fig. 18: *Position and position error responses of tilt joint (coupled tracking)*

5.3 Kinematic Model-based Decoupling Controller Design for Lift-Tilt 2DOF System

A simplified model for hydraulic cylinder drive is that cylinder velocity is proportional to valve input:

$$\begin{aligned} \dot{z}_2 &= K_{\text{qa\_cyl2}} \cdot u_2 \\ \dot{z}_3 &= K_{\text{qa\_cyl3}} \cdot u_3 \end{aligned} \tag{15}$$

where $K_{\text{qa\_cyl}}$ is the cylinder velocity gain in actuator space.

Lift joint (rotational) velocity $\dot{\theta}_2$ is a function of lift cylinder velocity $\dot{z}_2$ and its joint geometry

$$\dot{\theta}_2 = \frac{1}{A_{\text{hLT11}}} \dot{z}_2 \tag{16}$$

From Eq. 5, 15 and 16, it can be derived that

$$\dot{\theta}_3 = \frac{1}{A_{\text{hLT22}}} K_{\text{qa\_cyl3}} \cdot u_3 - \frac{A_{\text{hLT21}}}{A_{\text{hLT22}}} \dot{\theta}_2 \tag{17}$$

Therefore, to eliminate the coupling term in Eq. 17, a model-based decoupling controller should be defined as

$$u_3 = C_3 \cdot \Delta\theta_3 + \frac{A_{\text{hLT21}}}{K_{\text{qa\_cyl3}}} \dot{\theta}_2 \tag{18}$$

where the first term in Eq. 18 is the position controller for tilt joint (in this case a phase-lag P-controller), the second term denotes the decoupling term (in this case velocity feedforward from lift joint). Furthermore, when cylinder velocity gain $K_{\text{qa\_cyl3}}$ is assumed to be constant, the decoupling term depends only on the kinematic parameters A_{hLT21}, which is derived from the kinematic model of Eq. 21.

With this kinematic model-based decoupling controller in Eq. 18, again, tilt angle is kept stationary and the tracking performances of both joints are analyzed ($\dot{\theta}_{\text{lift}} = \pm$ 0.1 deg/s, $\dot{\theta}_{\text{tilt}} = 0$ deg/s). Figures 19 and 20 show the position and position error responses of both joints. It can be seen that the tracking errors are less than ± 0.03 deg for lift joint (velocity/tracking error = 3.3 deg/s/deg), and the tracking errors of tilt joint are less than ± 0.02 deg (velocity/tracking error = 5 deg/s/deg), which are 5 times smaller than the coupled case in Fig. 18.

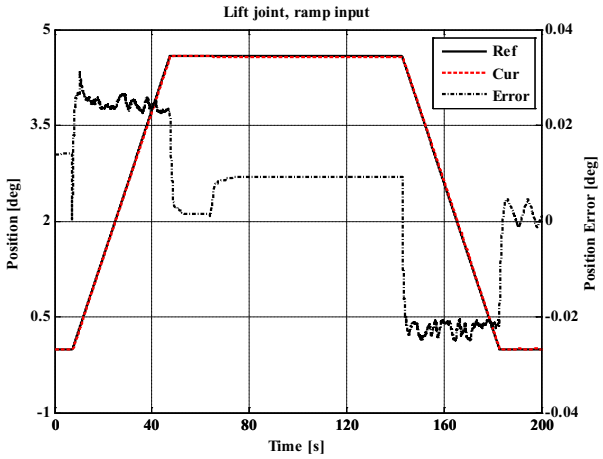

Fig. 19: *Position and position error responses of lift joint (decoupled tracking)*

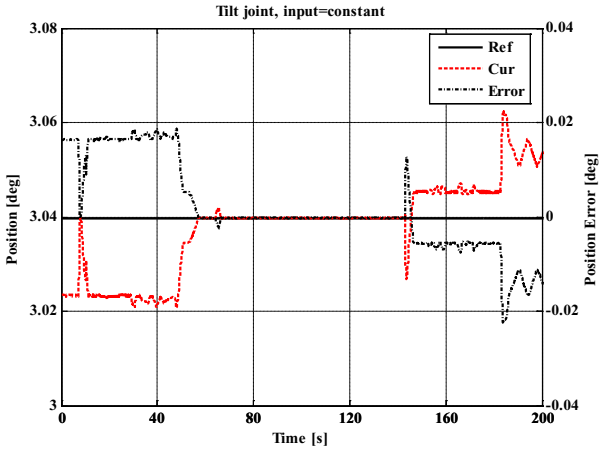

Fig. 20: *Position and position error responses of tilt joint (decoupled tracking)*

5.4 Controller Design for CRO-HRO 2DOF System

Based on the estimation in section 5.1, phase lag controller can still be applied to HRO joint, however, the available position open loop gain K of CRO joint is limited by the rather low natural frequency (1 Hz). To increase the open loop gain K, one effective way is

to increase the damping ratio δ_n using acceleration feedback K_a (as shown in Fig. 21).

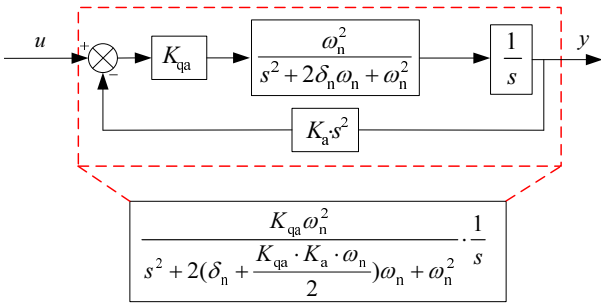

Fig. 21: *Hydraulic actuator model with acceleration feedback*

The effective damping ratio with acceleration feedback is expressed as

$$\delta = \delta_n + \frac{K_{qa}\cdot K_a\cdot\omega_n}{2} \qquad (19)$$

In this case, the effective damping ratio is tuned to be 0.5, and the corresponding position loop gain is increased twice.

The chosen lowest natural frequency for HRO phase lag P-controller design is 3 Hz, which can significantly decrease the coupling effects and still achieve desired steady-state accuracy. The controller gains for CRO and HRO joints are listed in Table 2.

The step responses of CRO joint with proportional controller and acceleration feedback controller are presented in Fig 22. It can be seen that the steady-state error of P-controller exceeds ± 0.05 deg. By contrast, acceleration feedback controller achieves faster responses and three times better accuracies (< ± 0.015 deg).

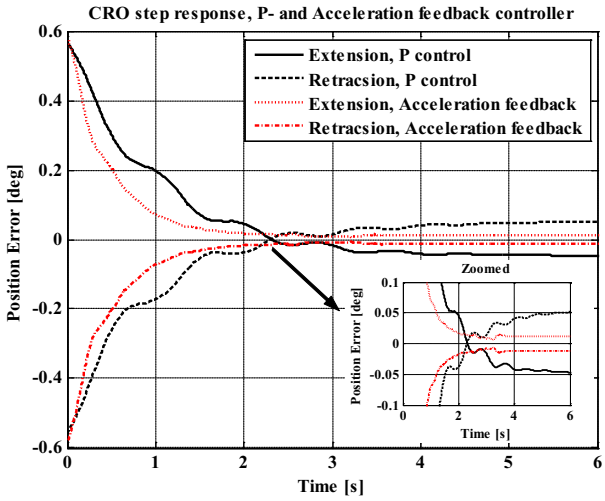

Fig. 22: *Position error responses of CRO joint (P- and acceleration feedback controller, step input)*

The step responses of HRO joint with phase lag P-controller are presented in Fig 23. The steady state position errors are less than .± 0.01 deg.

To improve the tracking performance individual velocity feedforward gains are tuned for CRO and HRO joints, $P_{d\text{CRO}}$ = 1.6 mA·s/deg, $P_{d\text{HRO}}$ = 2.1 mA·s/deg. Figures 24 and 25 show the tracking performances of both joints with sinusoidal inputs ($\bar{v}$ = 0.3 deg/s)

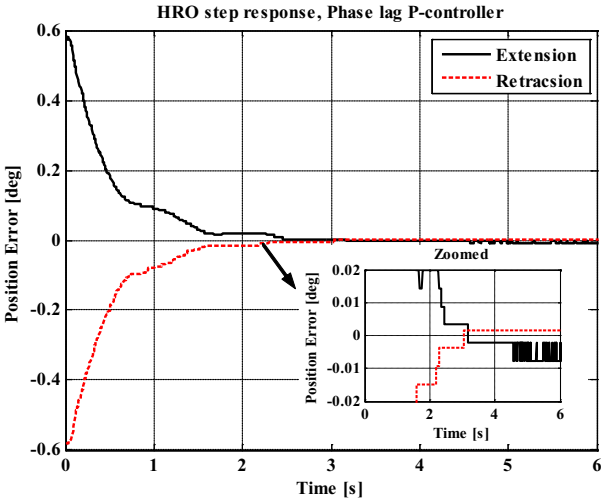

Fig. 23: *Position error responses of HRO joint (P-controller, step)*

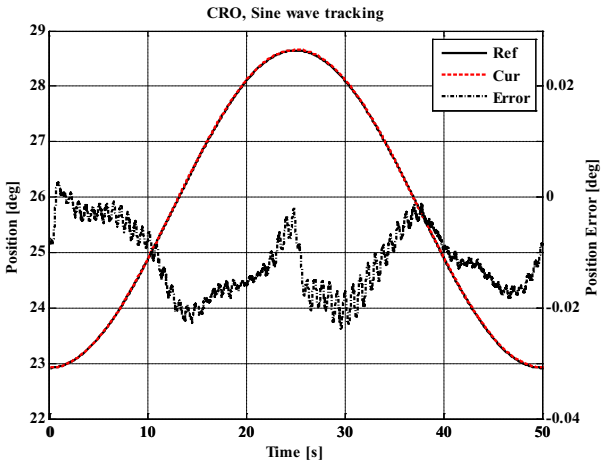

Fig. 24: *Position and position error responses of CRO joint (Sine wave tracking)*

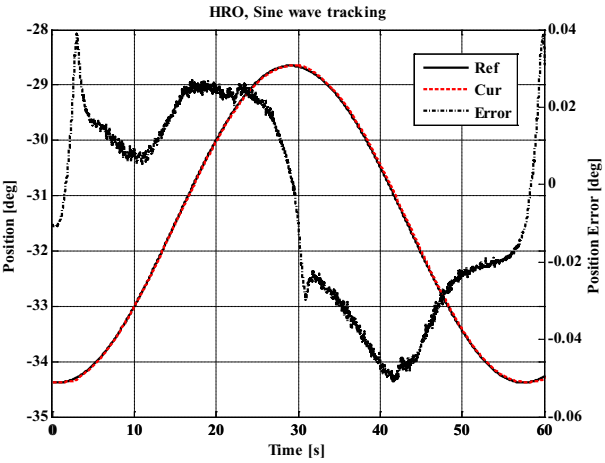

Fig. 25: *Position and position error responses of HRO joint (Sine wave tracking)*

The tracking errors of CRO joint are less than ± 0.03 deg (velocity/tracking error = 10 deg/s/deg),

while the errors are less than ± 0.05 deg for HRO joint (velocity/tracking error = 7.5 deg/s/deg).

6 Conclusion

Decentralized approach is used for individual joint controller design, resulting in phase lag P-controllers for the lift, tilt and HRO joints and acceleration feedback controller for the CRO joint. The performances of corresponding controller design are evaluated by step and waveform inputs. Due to the kinematic coupling effect of lift joint, poor tracking performance is observed in tilt joint. Consequently, a model-based decoupling controller is designed and tested, achieving five times smaller tracking errors. For each joint, the achieved steady state accuracy is better than ± 0.02 deg, and follow-up accuracy is better than ± 0.05 deg. In the ideal case (no manufacturing tolerances, no uncertainties in deflections), ± 5 mm positioning accuracy can be reached at the farthest point of the cassette in Cartesian space. Therefore, this study confirms that in spite of using commercially available water hydraulic components, the achieved positioning accuracies and dynamic behavior are competitive with their oil hydraulic counterpart.

Currently the study of fault tolerant control of this manipulator is being carried out. The durability of crucial water hydraulic components, such as servo valve, is also important and needs to be tested in the future. At very low speed, the nonlinear friction force causes stick-slip in cylinder motion, which may need friction modelling and compensation.

Acknowledgements

This work, supported by the European Communities under the contract of Association between EURATOM/TEKES, was carried out within the framework of the European Fusion Development Agreement. The views and opinions expressed herein do not necessarily reflect those of the European Commission.

Nomenclature

A_1	Area of cylinder piston side	[m^2]
A_2	Area of cylinder rod side	[m^2]
$\boldsymbol{A}_i^{i-1}$	Homogeneous transformation matrix	[-]
$\boldsymbol{A}_h$	Joint-to-actuator Jacobian matrix	[-]
$\boldsymbol{A}_{h0}$	Joint-to-actuator Jacobian matrix at the linearization point	[-]
$\boldsymbol{A}_{hLT}$	Joint-to-actuator Jacobian matrix for LIFT and TILT joints	[-]
$\boldsymbol{A}_{hCH}$	Joint-to-actuator Jacobian matrix for CRO and HRO joints	[-]
$\boldsymbol{F}_h$	Vector of cylinder forces with friction force	[-]
F_L	External force	[N]
$\boldsymbol{G}$	Vector of gravitational torque	[-]
$\boldsymbol{G}_{LT}$	Vector of gravitational torque for lift-tilt 2DOF system	[-]
$\boldsymbol{G}_{CH}$	Vector of gravitational torque for CRO-HRO 2DOF system	[-]
H	Valve hysteresis	[%]
$\boldsymbol{J}$	Joint-to-Cartesian Jacobian matrix	[-]
$\boldsymbol{J}_P^{(l_i)}$	Jacobian of link i	[-]
K	Position open loop gain	[1/s]
$\boldsymbol{K}$	Stiffness matrix	[-]
$\boldsymbol{K}_0$	Stiffness matrix at the linearization point	[-]
K_a	Acceleration feedback gain	[mA·s^2/deg]
K_{hj}	Spring constant of cylinder j	[N/m]
K_{pg}	Pressure gain of the servo valve	[bar/mA]
K_{qa}	Velocity gain in joint space	[deg/s/mA]
K_{qa_in}	Retracting velocity gain in joint space	[deg/s/mA]
K_{qa_cyl}	Velocity gain in actuator space	[m/s/mA]
K_{qa_out}	Extending velocity gain in joint space	[deg/s/mA]
KP	P-controller gain	[mA/deg]
KP_{des}	Desired position loop gain	[mA/deg]
KP_p	P-controller gain in extension direction	[mA/deg]
KP_n	P-controller gain in retraction direction	[mA/deg]
M	Mass of the cassette	[kg]
$\boldsymbol{M}$	Inertia matrix	[-]
$\boldsymbol{M}_0$	Inertia matrix at the linearization point	[-]
$\boldsymbol{M}_{LT}$	Inertia matrix for lift-tilt 2DOF system	[-]
$\boldsymbol{M}_{CH}$	Inertia matrix for CRO-HRO 2DOF system	[-]
$\boldsymbol{P}_{Ci}$	Position vector of link i	[-]
P_d	Speed feedforward gain	[mA·s/deg]
p_S	Supply pressure	[bar]
Q_N	Nominal flow rate	[m^3/s]
$\boldsymbol{V}$	Centrifugal and Coriolis terms matrix	[-]
a_i	Length of link i	[m]
d_i	Translational distance between two incident normals of a joint axis	[m]
f	Natural frequency	[Hz]
g_0	Gravity acceleration vector in the base frame	[-]
$\boldsymbol{h}_1$	Joint-to-Cartesian position transformation matrix	[-]
$\boldsymbol{h}_2$	Joint-to-actuator position transformation matrix	[-]
m_{li}	Mass of link i	[kg]
u	Valve input	[mA]
u_i	Valve input of cylinder i	
u_{max}	Rated valve input	[mA]
$\boldsymbol{v}$	Velocity vector in Cartesian coordinate	[-]
$\boldsymbol{y}$	Position vector in Cartesian	[-]

	coordinate	
z_i	Link length of cylinder i	[m]
$\dot{z}_i$	Velocity of cylinder i	[m/s]
$\boldsymbol{z}$	Vector of cylinder length	[-]
$\dot{\boldsymbol{z}}$	Vector of cylinder velocity	[-]
δ	Effective damping ratio	[-]
δ_n	Damping ratio	[-]
Δp_N	Nominal pressure drop	[bar]
Δy	Position error	[deg]
α_i	Twist angle between two adjacent joint axes,	[rad]
θ_i	Angle of joint i	[rad]
$\dot{\theta}_i$	Angular velocity of joint i	[rad/s]
$\boldsymbol{\theta}$	Vector of joint angle	[-]
$\dot{\boldsymbol{\theta}}$	Vector of joint angular velocity	[-]
$\lambda_k\{\cdot\}$	*k*:th eigenvalue of square matrix	[-]
τ_i	Time constant of phase lag P control	[s]
$\boldsymbol{\tau}$	Vector of joint torque	[-]
ω_{BW}	Desired bandwidth	[rad/s]
ω_n	Natural frequency	[rad/s]
ω_k	*k*:th natural frequency	[rad/s]

References

Davliakos, **I.** and **Papadopoulos**, **E.** 2008. Model-based control of a 6-dof electrohydraulic Stewart-Gough platform. *Mechanism and Machine Theory*, Vol. 43(11), pp. 1385-1400.

Edge, K. A. and **Gomes de Almeida**, **F.** 1995. Decentralized adaptive control of a directly driven hydraulic manipulator. Part 1: theory. *Proceedings of the Institution of Mechanical Engineers, Part I: Journal of Systems and Control Engineering*, Vol. 209(I3), pp. 191-196.

Gizatullin, **A. O.** and **Edge**, **K. A.** 2006. Adaptive control for a multi-axis hydraulic test rig. *Proceedings of the Institution of Mechanical Engineers, Part I: Journal of Systems and Control Engineering*, Vol. 221(2), pp. 183-198.

Gunnarsson, **S.** and **Krus**, **P.** 1994. LQG control of a flexible mechanical structure using hydraulic actuators. *Proceeding of the 6th Bath International Fluid Power Workshop*, Bath, UK, pp. 280-294.

Guo, **H.**, **Liu**, **Y.**, **Liu**, **G.** and **Li**, **H.** 2008. Cascade control of a hydraulically driven 6-DOF parallel robot manipulator based on sliding mode. *Control Engineering Practice*, Vol. 16(9), pp. 1055-1068.

Linjama, **M.** 1998. *The Modelling and Actuator Space Control of Flexible Hydraulic Cranes.* PhD thesis. Tampere University of Technology.

Linjama, **M.** 1999. Analysis of multi-input-multi-output nature of hydraulic cranes. *Proceedings of Bath Workshop on Power Transmission and Motion Control*, Bath, UK, pp. 15-29.

Merritt, **H. E.** 1967. *Hydraulic Control Systems*. John Wiely & Sons, Inc.

Palmer, **J.**, **Siuko**, **M.**, **Agostini, P.**, **Gottfried**, **R.**, **Irving, M.**, **Martin**, **E.**, **Tesini**, **A.** and **Van Uffelen**, **M.** 2005. Recent developments towards ITER 2001 divertor maintenance. *Fusion Engineering and Design*, Vol. 75-79, pp. 583-587.

Plummer, **A. R.** 2004. Design optimization for parallel servohydraulic mechanisms. *Proceedings of Bath Workshop on Power Transmission and Motion Control*, Bath, UK, pp. 223-240.

Plummer, **A. R.** 2007. Motion control for overconstrained parallel servohydraulic mechanisms. *Proceedings of the 10th International Conference on Fluid Power*, Tampere, Finland.

Raneda, **A.**, **Pessi, P.**, **Siuko**, **M.**, **Handroos**, **H.**, **Palmer**, **J.** and **Vilenius**, **M.** 2003. Utilization of virtual prototyping in development of CMM. *Fusion Engineering and Design*, Vol. 69, pp. 183-186.

Rebut, **P. H.** 1995. ITER: the first experimental fusion reactor. *Fusion Engineering and Design*, Vol. 27, pp. 3-16.

Sciavicco, **L.** and **Siciliano**, **B.** 2000. *Modelling and Control of Robot Manipulators (2nd edition)*. Springer.

Sirouspour, **M.** and **Salcudean**, **S.** 2001. Nonlinear control of hydraulic robots. *IEEE Transactions of Robotics and Automation*, Vol. 17(2), pp. 173-182.

Tsai, **L.** 1999. *Robot Analysis : the Mechanics of Serial and Parallel Manipulators*. John Wiley & Sons, Inc.

Virvalo, **T.** 2001. PI and PID-controllers in a hydraulic position servo system – What it is all about?. *Proceedings of the 5th International Conference on Fluid Power Transmission and Control*, Hangzhou, China.

Virvalo, **T.** and **Mattila**, **J.** 2007. Follow-up accuracy of water hydraulic swing. *Proceedings of the 5th International Symposium on Fluid Power Transmission and Control*, Beidaihe, China.

Appendix

Variable definitions

For the derivation of the kinematic and dynamic equations, the schematic diagram in Fig. 2 is used with variables defined as follows:

$L_1 = \overline{AD} = 1.080$ m $m_3 = 371$ kg
$L_2 = \overline{GJ} = 0.376$ m $m_4 = 89$ kg
$a_{22} = \overline{AF} = 0.975$ m $M = 9000$ kg
$a_{23} = \overline{AE} = 1.024$ m $\varphi_1 = \angle BAF = 5.48°$
$a_{33} = \overline{BC} = 1.134$ m $\varphi_2 = \angle ADz_0 - axis = 100°$
$a_{44} = \overline{GK} = 0.349$ m $\varphi_3 = \angle CBO_3 = 78.8°$
$a_{45} = \overline{GL} = 0.613$ m $\varphi_4 = \angle EAz_0 - axis = 21.2°$

$a_{55} = \overline{HI} = 0.386$ m $\quad \varphi_5 = \angle MBO_3 = 10.5°$
$r_2 = \overline{Bm_2} = 0.856$ m $\quad \varphi_6 = \angle m_2 BO_3 = 29.8°$
$r_3 = \overline{Gm_3} = 0.216$ m $\quad \varphi_7 = \angle LHI = 77.4°$
$r_4 = \overline{Hm_4} = 0.154$ m $\quad \varphi_8 = \angle JGH = 74.3°$
$R_1 = \overline{BM} = 2.662$ m $\quad \varphi_9 = \angle m_3 GH = 12.2°$
$R_2 = HM = 1.082$ m $\quad \varphi_{10} = \angle m_4 HN = 47.4°$
$m_1 = 306$ kg $\quad \varphi_{11} = \angle m_4 HM = 0°$
$m_2 = 1250$ kg $\quad \varphi_{13} = \angle KGy_0 - axis = 13.2°$
$z_2 = \overline{EF}$ = lift cylinder length
$z_3 = \overline{DC}$ = tilt cylinder length
$z_4 = \overline{KL}$ = CRO cylinder length
$z_5 = \overline{JI}$ = HRO cylinder length

Kinematics of the Lift-tilt 2DOF System

The joint-to-actuator transformation and corresponding differential kinematic equations are derived as

$$z_2 = \sqrt{a_{22}^2 + a_{23}^2 - 2a_{22}a_{23}\cos(\theta_2 - \varphi_1 + \varphi_4)}$$
$$z_3 = \sqrt{\begin{matrix} L_1^2 + 2L_1 a_{33}\cos(\varphi_2 - \theta_2 - \theta_3 + \varphi_3) + a_2^2 + a_{33}^2 \\ +2a_2 a_{33}\cos(\varphi_3 - \theta_3) + 2L_1 a_2 \cos(\varphi_2 - \theta_2) \end{matrix}} \quad (20)$$

$$\begin{bmatrix} \dot{z}_2 \\ \dot{z}_3 \end{bmatrix} = \begin{bmatrix} A_{\mathrm{hLT11}} & 0 \\ A_{\mathrm{hLT21}} & A_{\mathrm{hLT22}} \end{bmatrix} \begin{bmatrix} \dot{\theta}_2 \\ \dot{\theta}_3 \end{bmatrix} \quad (21)$$

where

$$\begin{aligned} A_{\mathrm{hLT11}} &= (a_{22}a_{23}\sin(\theta_2 - \varphi_1 + \varphi_4))/z_2 \\ A_{\mathrm{hLT12}} &= 0 \\ A_{\mathrm{hLT21}} &= (L_1 a_2 \sin(\varphi_2 - \theta_2) + L_1 a_{33}\sin(\varphi_2 - \theta_2 \\ &\quad -\theta_3 + \varphi_3))/z_3 \\ A_{\mathrm{hLT22}} &= (L_1 a_{33}\sin(\varphi_2 - \theta_2 - \theta_3 + \varphi_3) + a_2 a_{33} \\ &\quad \sin(\varphi_3 - \theta_3))/z_3 \end{aligned} \quad (22)$$

Kinematics of the CRO-HRO 2DOF System

The joint-to-actuator transformation and corresponding differential kinematic equations are expressed as

$$z_4 = \sqrt{\begin{matrix} a_{44}^2 + a_{45}^2 - 2a_{44}a_{45}\cos(\pi/2 - \varphi_8 + \theta_4 \\ +\varphi_{12} + \varphi_{13}) \end{matrix}}$$
$$z_5 = \sqrt{\begin{matrix} L_2^2 - 2L_2 a_4 \cos(\varphi_8) + a_4^2 + a_5^2 + 2a_4 a_5 \\ \cos(\varphi_7 - \theta_5) - 2L_2 a_5 \cos(\varphi_8 - \varphi_7 + \theta_5) \end{matrix}} \quad (23)$$

$$\begin{bmatrix} \dot{z}_4 \\ \dot{z}_5 \end{bmatrix} = \begin{bmatrix} A_{\mathrm{hCH11}} & 0 \\ 0 & A_{\mathrm{hCH22}} \end{bmatrix} \begin{bmatrix} \dot{\theta}_4 \\ \dot{\theta}_5 \end{bmatrix} \quad (24)$$

where

$$\begin{aligned} A_{\mathrm{hCH11}} &= (a_{44}a_{45}\sin(\pi/2 - \varphi_8 + \theta_4 + \varphi_{12} + \varphi_{13}))/z_4 \\ A_{\mathrm{hCH22}} &= (L_2 a_5 \sin(\pi - \varphi_8 - \theta_5 + \varphi_7) + a_4 a_5 \sin(\varphi_7 \\ &\quad -\theta_5))/z_5 \end{aligned} \quad (25)$$

Dynamics of the Lift-tilt 2DOF System

For the lift-tilt 2DOF system, the terms of the dynamic equation are derived at 0 rotation of the cassette, which is regarded as the worst case scenario of the vibration modes analysis. The inertia matrix and gravitational torque vector are derived based on Eq. 8 and 9

$$\boldsymbol{M}_{\mathrm{LT}} = \begin{bmatrix} M_{\mathrm{LT11}} & M_{\mathrm{LT12}} \\ M_{\mathrm{LT21}} & M_{\mathrm{LT22}} \end{bmatrix} \quad (26)$$

$$\begin{aligned} M_{\mathrm{LT11}} &= m_1 r_1^2 + m_2(a_2^2 + 2a_2 r_2 \cos(\theta_3 - \varphi_6) \\ &\quad +r_2^2) + M(a_2^2 + 2a_2 R_1 \cos(\theta_3 + \varphi_5) + R_1^2) \\ M_{\mathrm{LT12}} &= m_2(a_2 r_2 \cos(\theta_3 - \varphi_6) + r_2^2) + M(a_2 \\ &\quad R_1 \cos(\theta_3 + \varphi_5) + R_1^2) \\ M_{\mathrm{LT21}} &= M_{\mathrm{LT12}} \\ M_{\mathrm{LT22}} &= m_2 r_2^2 + MR_1^2 \end{aligned} \quad (27)$$

$$\boldsymbol{G}_{\mathrm{LT}} = \begin{bmatrix} G_{\mathrm{LT1}} & G_{\mathrm{LT2}} \end{bmatrix}^{\mathrm{T}} \quad (28)$$

$$\begin{aligned} G_{\mathrm{LT1}} &= m_1 g r_1 \sin(\theta_2) + m_2 g(a_2 \cos(\theta_2) + r_2 \\ &\quad \cos(\theta_2 + \theta_3 - \varphi_6)) + Mg(a_2 \cos(\theta_2) + R_1 \\ &\quad \cos(\theta_2 + \theta_3 + \varphi_5)) \\ G_{\mathrm{LT2}} &= m_2 r_2 g \cos(\theta_2 + \theta_3 - \varphi_6) + MR_1 g \\ &\quad \cos(\theta_2 + \theta_3 + \varphi_5) \end{aligned} \quad (29)$$

Dynamics of the CRO-HRO 2DOF System

Similarly, the inertia matrix and gravitational torque vector for CRO-HRO 2DOF system are derived as follows.

$$\boldsymbol{M}_{\mathrm{CH}} = \begin{bmatrix} M_{\mathrm{CH11}} & M_{\mathrm{CH12}} \\ M_{\mathrm{CH21}} & M_{\mathrm{CH22}} \end{bmatrix} \quad (30)$$

$$\begin{aligned} M_{\mathrm{CH11}} &= m_3 r_3^2 + m_4(a_4^2 + 2a_4 r_4 \cos(\theta_5 - \varphi_{10}) \\ &\quad +r_4^2) + M(a_4^2 + 2a_4 R_2 \cos(\theta_5 - \varphi_{11}) + R_2^2) \\ M_{\mathrm{CH12}} &= m_4(a_4 r_4 \cos(\theta_5 - \varphi_{10}) + r_4^2) + M \\ &\quad (a_4 R_2 \cos(\theta_5 - \varphi_{11}) + R_2^2) \\ M_{\mathrm{CH21}} &= M_{\mathrm{CH12}} \\ M_{\mathrm{CH22}} &= m_4 r_4^2 + MR_2^2 \end{aligned} \quad (31)$$

$$\boldsymbol{G}_{\mathrm{CH}} = \begin{bmatrix} 0 & 0 \end{bmatrix}^{\mathrm{T}} \quad (32)$$

Likui Zhai
Born in Xintai, China, 1981, he received his BS and MS in mechanical engineering from Nanjing University of Sci & Tech (China) in 2004 and Zhejiang University (China) in 2006 respectively. He is now a postgraduate student in Tampere University of Technology (Finland). His main research fields are modelling and control of electrohydraulic servo system.

Tapio Virvalo
He received his MS in mechanical engineering from Helsinki University of Technology, Finland in 1967, and PhD degree from Tampere University of Technology, Finland in 1995. He is presently as the professor of machine automation in Department of Intelligent Hydraulics and Automation (IHA) at Tampere University of Technology. His current research interests are motion control, especially, in fluid power applications including pneumatics and water hydraulics. His long term interests have also been in mechatronics and control engineering.

Jouni Mattila
He received his PhD degree (2000) in mechanical engineering from Tampere University of Technology. At present he is a senior researcher and project manager of FUSION/DTP2 in Department of Intelligent Hydraulics and Automation (IHA) at Tampere University of Technology. His research interests have been in robotics and control engineering.

Hannu Saarinen
Born in Finland, 1967. He received his MS (1993) in mechanical engineering from Tampere University of Technology. Currently he is a senior research scientist working at the ROVIR team of VTT, where he is coordinating the tasks for designing and developing CMM control software. His scientific interests include robotics, virtual reality and real-time control systems.